

RACR-MIL: Rank-aware contextual reasoning for weakly supervised grading of squamous cell carcinoma using whole slide images

Anirudh Choudhary^a, Mosbah Aouad^a, Krishnakant Saboo^a, Angelina Hwang^b, Jacob Kechter^b, Blake Bordeaux^b, Puneet Bhullar^b, David DiCaudo^b, Steven Nelson^b, Nneka Comfere^c, Emma Johnson^c, Olayemi Sokumbi^d, Jason Sluzevich^b, Leah Swanson^b, Dennis Murphree^c, Aaron Mangold^b, Ravishankar Iyer^a

^aUniversity of Illinois Urbana-Champaign, Champaign, 61820, IL, USA

^bMayo Clinic, 13400 E. Shea Blvd. Scottsdale, Scottsdale, 85259, AZ, USA

^cMayo Clinic, 200 1st St SW, Rochester, Rochester, 55905, MN, USA

^dMayo Clinic, 4500 San Pablo Rd S, Jacksonville, 32224, FL, USA

Abstract

Squamous cell carcinoma (SCC) is the most common cancer subtype, with an increasing incidence and a significant impact on cancer-related mortality. SCC grading using whole slide images is inherently challenging due to the lack of a reliable protocol and substantial tissue heterogeneity. We propose RACR-MIL, the first weakly-supervised SCC grading approach achieving robust generalization across multiple anatomies (skin, head & neck, lung). RACR-MIL is an attention-based multiple-instance learning framework that enhances grade-relevant contextual representation learning and addresses tumor heterogeneity through two key innovations: (1) a hybrid WSI graph that captures both local tissue context and non-local phenotypical dependencies between tumor regions, and (2) a rank-ordering constraint in the attention mechanism that consistently prioritizes higher-grade tumor regions, aligning with pathologists' diagnostic process. Our model achieves state-of-the-art performance across multiple SCC datasets, achieving 3-9% higher grading accuracy, resilience to class imbalance, and up to 16% improved tumor localization. In a pilot study, pathologists reported that RACR-MIL improved grading efficiency in 60% of cases, underscoring its potential as a clinically viable cancer diagnosis and grading assistant.

Keywords: Computational pathology, Weakly supervised learning, Squamous cell cancer, Multiple instance learning, Graph neural network, Rank ordering

1. Introduction

Squamous cell carcinoma (SCC) is the most common cancer subtype and a major cause of cancer-related mortality (Tokez et al. (2020)). It affects multiple anatomies, including the skin, head and neck, and lungs, with skin SCC being the most prevalent (≈ 1 million cases annually (Tokez et al. (2020); Rogers et al. (2015))). Accurate histopathological tumor grading from whole slide images (WSI) is crucial for assessing SCC severity and informing patient prognosis. However, this task remains challenging due to significant intratumoral heterogeneity, subtle morphological variations between grades and the lack of a standardized, reliable protocol for SCC (Diede et al. (2024)). Pathologists typically assess SCC grade by integrating local tumor morphology and cellular differentiation with broader contextual cues, such as tumor growth pattern, keratinization, and tumor microenvironment.

Weakly-supervised learning, which leverages WSI-level label instead of pixel-level annotations, has emerged as a promising paradigm for automated cancer grading (Dominguez-Morales et al. (2024)). However, existing weakly-supervised methods often fail to explicitly model the heterogeneous tissue dependencies considered by clinicians and lack mechanisms to consistently emphasize diagnostically critical high-grade tumor regions. As a result, regions with varying grades are treated equivalently, resulting in a diffused model focus (Figure 1). Our goal is to develop a weakly supervised SCC grading approach using tissue-level label, to classify WSI into one of four grading classes:

*Corresponding author. E-mail address: ac67@illinois.edu, Phone: +1-6462514328 (Anirudh Choudhary)

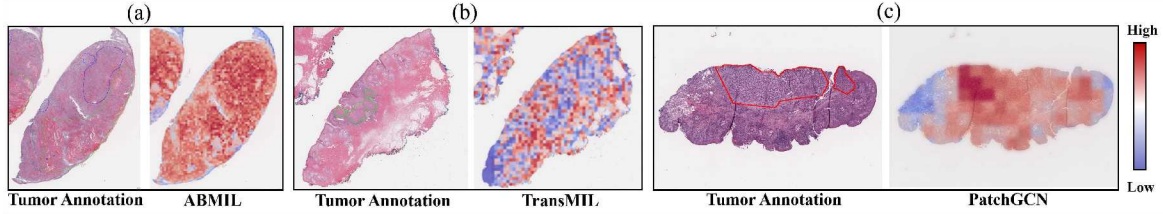


Figure 1: Attention heatmaps for existing MIL methods with corresponding tumor annotations (Red: Poor, Blue: Moderate, Green: Well): (a) ABMIL without ranking constraint fails to consistently rank tumor regions assigning similar importance to Moderately-differentiated and Well-differentiated regions; (b) Transformer-based approach (TransMIL) is susceptible to tissue noise leading to false positives and misses the relevant tumor region; (c) Graph convolutional network (PatchGCN) suffers from oversmoothing and assigns similar importance to tumor and non-tumor regions, failing to prioritize relevant local information.

normal (no tumor), well-differentiated, moderately-differentiated, and poorly-differentiated. To our knowledge, this is the first AI-based SCC grading approach designed to achieve robust generalization across multiple anatomical sites (skin, head and neck, lung). Our framework incorporates a novel graph representation learning approach to capture clinically relevant tissue context and handles tumor heterogeneity through a ranking-based formulation, prioritizing diagnostically relevant regions.

We address the grading task using attention-based multiple-instance learning (MIL), leveraging its success in prior cancer grading studies (Mun et al. (2021); Silva-Rodriguez et al. (2021); Otálora et al. (2021)). Attention-based MIL faces three key challenges in SCC. First, SCC WSIs often comprise heterogeneous tumor regions; pathologists implicitly rank these regions, prioritizing the higher-grade tumor regions during diagnosis (Prezzano et al. (2021)). Current methods do not enforce the ranking constraints in the attention-based formulation, resulting in over-emphasis on low-grade regions and suboptimal tumor localization (Dominguez-Morales et al. (2024)). Second, SCC grading is influenced by tissue contextual dependencies, such as tumor growth pattern and tumor microenvironment structure (e.g., keratinization, inflammatory response (Diede et al. (2024))). Existing studies either analyze patches independently, ignoring contextual information (Silva-Rodriguez et al. (2021); Mun et al. (2021)) or rely on graph networks and transformers to model dependencies (Behzadi et al. (2024)). Transformer-based methods (e.g., TransMIL (Shao et al. (2021))) excel at capturing long-range context but are prone to assigning non-zero weights to biologically irrelevant regions due to their dense attention formulation. This dilutes fine-grained morphological differences and makes it susceptible to noisy tissue structures, leading to suboptimal performance (Figure 1). Graph-based approaches efficiently propagate information through explicit edges. However, traditional GNN approaches (e.g., PatchGCN (Chen et al. (2021))) which rely on spatial proximity, struggle to capture long-range context due to shallow network depth and inability to prioritize relevant neighbors (Figure 1). Third, the limited size and imbalance of training data, with fewer high-grade cases encountered in clinical settings, further exacerbates these challenges, causing overfitting. To overcome these challenges, we propose an approach that utilizes rank-aware contextual reasoning (RACR) to leverage tumor contextual information and emulate the ordinal grading protocol followed by pathologists.

Our model, RACR-MIL, presents two key innovations. First, we introduce a two-part rank-ordering constraint on the attention network: (i) an *inter-grade* constraint, which prioritizes more severe tumor patches across different grades, and (ii) an *intra-grade* constraint, which prioritizes more probable patches within the same grade. Rank ordering enables our model to consistently assign higher importance to the most severe tumor regions, aligning the aggregated feature and prediction with the overall label and improving tumor localization.

Second, we define a hybrid dual graph on WSI that captures both short- and long-range contextual dependencies relevant to SCC grading. The dual graph formulation captures complementary relationships with distinct structural priors: (i) a *latent graph* that sparsely connects phenotypically similar WSI regions (e.g., scattered tumor nests) based on feature similarity, enabling the modeling of structural patterns associated with tumor growth; and (ii) a *spatial graph* based on physical proximity which encodes local structure relations in tumor’s immediate microenvironment, such as keratinization and immune infiltration. We apply graph diffusion to strengthen higher-order interactions in the latent graph and use transformer-based self-attention to adaptively weigh relations (edges) in both graphs. To encourage complementary contextual information across spatial and latent dimensions, a diversity constraint is

imposed to promote distinct relational patterns across the two graphs. This dual-graph design improves the model’s capacity to capture fine-grained morphological features while maintaining global tissue contextual understanding.

We comprehensively evaluate our approach across three squamous cancers, including skin SCC, head & neck SCC, and lung SCC, and compare with state-of-the-art weakly-supervised methods. RACR-MIL outperforms existing MIL methods, achieving a 3-9% improvement in grade classification and 5-20% higher accuracy on challenging higher-grade tumors. Our approach successfully localizes diagnostically important tumor regions with up to 16% higher sensitivity compared to existing methods. Qualitative analysis of tumor heatmaps for skin SCC reveals greater alignment with clinicians’ annotations and consistent importance assigned to tumor regions of interest. To summarize, our contributions are as follows:

1. We propose the first weakly supervised framework for multiclass SCC grading using a dual graph formulation to jointly model spatial and phenotypic context, encouraging each graph to capture complementary information relevant to grading.
2. We introduce a rank-aware attention mechanism that explicitly prioritizes worse-grade regions, mimicking the implicit grading hierarchy followed by pathologists.
3. Our innovations lead to state-of-the-art performance in tumor grade classification and achieve greater alignment with pathologists’ annotations, both qualitatively and quantitatively. Additionally, a small-scale pilot evaluation of RACR-MIL’s efficacy as a grading assistant by pathologists supports its potential for clinical translation.
4. We demonstrate strong generalization and enhanced robustness across diverse anatomical sites, with increased resilience to class imbalance and reduced performance variability across evaluation data folds.

2. Related Work

Weakly-supervised grading: Most weakly-supervised grading studies focus on non-SCC cancers, particularly Gleason grading in prostate cancer. For prostate cancer, studies can be broadly categorized into: (i) methods that incorporate weak tissue-level annotations along with slide-level grade labels (Kanavati et al. (2020); Otálora et al. (2021)), and (ii) approaches that rely solely on WSI-level Gleason or ISUP grades (Mun et al. (2021); Silva-Rodriguez et al. (2021)). Otálora et al. (2021) demonstrated the utility of combining limited patch-level supervision with large-scale weak labels via a transfer learning-based MIL strategy. Silva-Rodriguez et al. (2021) used max-pooling MIL to derive pseudo-patch labels from WSI-level annotations, which are then used to train patch-level classifier. Mun et al. (2021) explore a two-stage non-contextual approach where the first-stage model classifies patches into cancer/benign, followed by attention-based MIL-based grading on pre-extracted features. Zhang et al. (2021) propose a non-contextual attention based MIL to sample patches at multiple magnification. A few works have applied graph neural networks (GNNs) for grading, but either use spatial graphs alone (Xiang et al. (2023)) or construct graph by selecting patches based solely on predicted tumor content (Behzadi et al. (2024)), potentially missing contextual information from tumor microenvironment. Myronenko et al. (2021) leverage transformer-based self-attention to capture instance dependencies and integrate a patch-level loss based on pseudo-labeling with their MIL architecture. However, comparative studies (Dominguez-Morales et al. (2024)) indicate that contextual MIL methods (e.g., TransMIL) perform only marginally better than non-contextual ones (e.g., CLAM-SB), highlighting the need for more effective contextual modeling in weakly-supervised grading. Recent studies have investigated weakly-supervised methods for skin cancers such as basal cell carcinoma (BCC). For instance, Yacob et al. (2023) introduced a graph-transformer architecture that integrates spatial graphs and transformer architecture to model both local and global contextual dependencies. Despite this, the method showed limited performance in differentiating higher-grade lesions. Similarly, Geijs et al. (2024) proposed StreamingCLAM for BCC risk stratification via end-to-end learning; however, the task was framed as binary by merging higher-grade classes, thereby limiting clinical granularity. In comparison, weakly supervised methods for SCC grading remain underexplored, with no existing work addressing the problem in a multiclass setting.

Attention-based multiple instance learning: Attention-based MIL (ABMIL) (Ilse et al. (2018)) introduced an attention mechanism with gating to aggregate patch-level features based on relevance. Subsequent extensions improved instance discrimination and representation. CLAM (Lu et al. (2021)) incorporated a SVM-inspired hinge loss at an instance-level to enhance separation between high- and low-attention patches, while its multiclass variant

(CLAM-MB) introduced class-specific attention heads. Li et al. (2021) propose a dual-stream MIL approach which learns instance- and embedding-level classifiers jointly and uses self-attention to model latent dependencies within the tissue.

Contextual MIL approaches: Graph-based methods explicitly capture spatial dependencies by representing image tiles as nodes with structured relationships. For example, Zheng et al. (2022) combine graph representations with transformer architecture for lung cancer subtyping, while Chen et al. (2021) propose PatchGCN which models local tissue structure through spatially resolved patch-level graphs. GCN-MIL (Xiang et al. (2023)) similarly constructs proximity-based graphs for prostate cancer grading. Li et al. (2024) extend this by dynamically defining graph edges using head and tail embeddings of patches, enabling adaptive spatial modeling. Beyond local relationships, several methods incorporate tumor heterogeneity and inter-tissue interactions for prognostic tasks. HEAT (Chan et al. (2023)) represent WSI as heterogeneous graph based on nuclear type relationships, and ProtoSurv (Wu et al. (2024)) integrates tissue category attributes into spatial graphs to distinguish between tissue structures. However, most of these methods rely heavily on spatial proximity for edge construction, limiting their ability to model long-range dependencies. To address this, Behzadi et al. (2024) propose a hybrid attention-based MIL framework that uses transformer self-attention to model patch relationships and identify salient regions, followed by GCNs to capture contextual information. However, using transformers to model dependencies between large number of patches might render them prone to noise. Transformer-based methods also incorporate spatial priors. for instance, TransMIL (Shao et al. (2021)) uses convolutional positional encodings. However, these approaches often rely on approximations such as Nystroformer, which can degrade performance. Our experiments suggest that dense self-attention mechanisms underperform on fine-grained tasks like tumor grading.

3. Methodology

Each WSI is represented as a bag b of patches $X_b = \{x_n\}_{n=1}^N$. N denotes the number of non-overlapping patches in a WSI, and $b \in \{1, 2 \dots B\}$, where B is the number of training samples. The patch-level labels y_n are unknown, and we have access only to the bag label $Y_b \in \{\text{normal, well, moderate, poor}\}$.

3.1. Tissue Feature Encoding

Tissue feature extraction consists of local feature extraction using self-supervised learning followed by contextual feature extraction using an attention-based dual graph convolution network.

3.1.1. Local feature extraction

We leverage self-supervised learning (SSL) to pre-train the patch feature extractor using unlabeled patches extracted from WSIs. To capture fine-grained pathological features (e.g., nuclei details, cell distribution, tumor microenvironment), we extract 448×448 sized non-overlapping patches at 20X magnification. The patch size and magnification were chosen to preserve high-resolution morphological details while ensure grading-relevant histological context within a single patch. We use Nest-S (Zhang et al. (2022)), a hierarchical transformer architecture, for efficient pretraining with larger-sized 448-dimensional images. We pretrain the feature extractor using DINO, a knowledge distillation-based SSL framework (Caron et al. (2021)).

After pretraining, the transformer network is used as an offline feature extractor to derive 384-dimensional feature $f_n \in \mathcal{R}^d$ for each patch x_n , leading to a WSI representation of $\{f_n\}_{n=1}^N$. Since the pre-trained features f_n are agnostic to the downstream task, we project them into a lower-dimensional space using a multi-layer perceptron (MLP) with nonlinear activation to get local patch features $h_n^0 \in \mathcal{R}^d$. The projection reduces noise and emphasizes grading-specific features, allowing the model to refine and adapt the pre-trained features. We jointly train the MLP along with the graph neural network, and the rank-aware grade classifier. Thus, the resulting local patch feature h_n^0 captures grading-specific information and de-emphasizes information irrelevant to the downstream task.

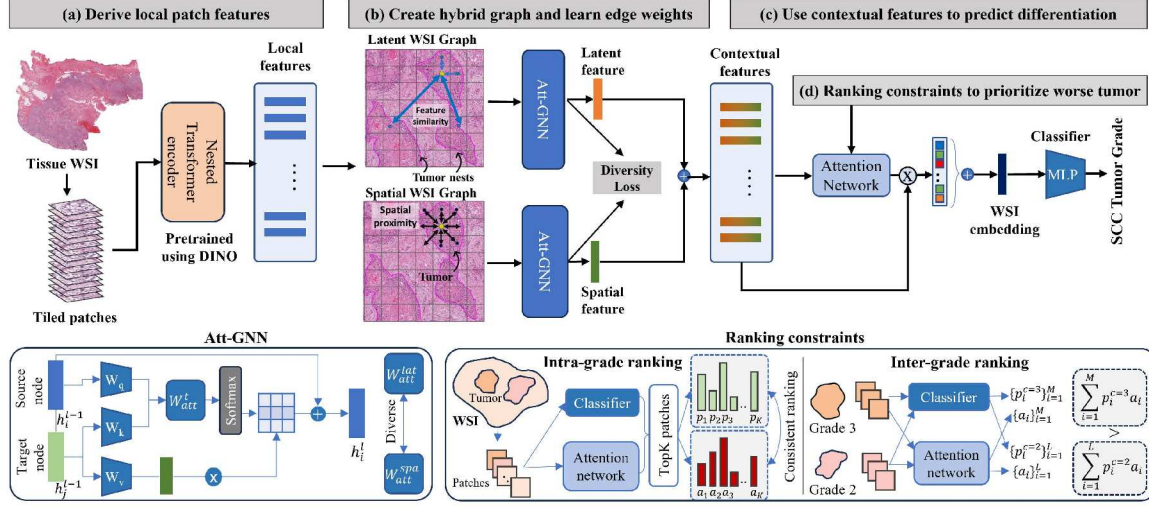


Figure 2: The proposed model. (a) Tissue tiling and local feature extraction. (b) Derivation of contextual patch features using self-attention-based graph convolution, taking latent and spatial semantic dependencies into account. (c) Prediction of grade using multiscale contextual features imposing a rank-order constraint on the attention network.

3.1.2. Contextual feature extraction

Although large, high-resolution patches capture localized context, they do not explicitly capture grade-relevant spatial relationships or long-range dependencies across tissue regions. To enhance contextual reasoning, we propose a hybrid graph formulation.

Hybrid graph construction: To derive contextual patch features capturing spatial and latent dependencies within the WSI, we construct an undirected hybrid graph for each WSI $G = (V, A)$ with patches as nodes V and edges between them defined using adjacency matrix $A \in \mathcal{R}^{N \times N}$. The edges capture the pathology-related structure and interdependence among tumor regions via two types of contextual dependencies incorporated in A : (i) A^{lat} , which represents non-local dependencies between phenotypically similar patches that can be spatially distant but are similar in terms of their morphology (grade) in the feature space; and (ii) A^{spa} , which captures local dependencies between a tumor patch and its spatially neighboring patches in the tumor microenvironment. This separation allows specialized modeling of distinct contextual dependencies and avoids the pitfalls of oversmoothing or diffuse attention. To ensure meaningful connectivity while maintaining sparsity, we construct k-nearest neighbors (kNN) graphs in both latent and spatial spaces.

Latent graph to capture phenotypic similarity: To define the latent dependency graph, we compute pairwise latent distance between patches using cosine distance-based feature similarity:

$$d_{ij}^{lat} = 1 - \frac{f_i \cdot f_j}{\|f_i\|_2 \|f_j\|_2} \quad (1)$$

where f_i and f_j represent features of patches i, j . We define latent edges connecting i^{th} patch to its k-nearest neighbors $j \in [1, N]$ that have the most similar features to that patch, i.e. $A_{ij}^{lat} = d_{ij}^{lat}$. Directly constructing a kNN-based latent graph introduces two limitations: (1) potential noise in edge formation due to suboptimal feature representations not finetuned for grading; and (2) limited ability to capture complex higher-order or long-range dependencies, as the graph is restricted to one-hop neighbors in the feature space. To address these issues, we adopt a two-step construction approach:

1. **Initial graph construction:** We first connect each patch to its k -nearest neighbors in the feature space ($k = 8$). To ensure robust connections, we define the set of k -reciprocal nearest neighbors $r_i(k)$ (Qin et al. (2011)) for each patch i as:

$$r_i(k) = j \in \mathcal{N}_k(i) \wedge i \in \mathcal{N}_k(j)$$

where $\mathcal{N}_k(i)$ denotes the set of the k -nearest neighbors of node i in the feature space. Reciprocal kNN takes into account the local density of feature vectors, ensuring that a latent edge is defined only if both patches mutually lie among each other's k -nearest neighbors. This reduces the impact of outliers in pretrained patch features.

2. **Refinement using graph diffusion:** We apply kernel-based graph diffusion to refine the initial latent graph and derive higher-order connections beyond one-hop neighbors. We use personalized PageRank Gasteiger et al. (2019) with random walk formulation to derive the diffused latent graph:

$$\hat{A}^{lat} = \sum_{k=0}^{\infty} \theta_k T^k \quad (2)$$

where $\theta_k = \alpha(1 - \alpha)^k$ with α being the probability of random jump to parent node ($\alpha = 0.25$), $T = A^{lat}D^{-1}$ is the normalized adjacency matrix where D is the diagonal matrix, $D = \sum_i A_{ii}^{lat}$. Graph diffusion results in a dense matrix \hat{A}_{ij} wherein edge weights represent the cumulative probability of reaching a target node based on feature similarity. Finally, we retain the top five neighbors per node based on their probability scores and truncate small values of \hat{A}_{ij} , recovering a sparse latent graph $\tilde{A}_{ij}^{lat} = \hat{A}_{ij}^{lat} > \delta$ where $\delta = 0.02$ is the sparsification threshold. As shown in Figure 3, graph diffusion amplifies short- and long-range connections between tumor regions and de-emphasizes noisy edges between morphologically distinct regions.

Spatial graph to capture local tissue relations: To define the spatial dependency graph, we connect each patch to its 8-nearest patches in the immediate vicinity based on the spatial distance.

$$d_{ij}^{spa} = \sqrt{(s_i - s_j)^2 + (t_i - t_j)^2} \quad (3)$$

where d_{ij}^{spa} represents the spatial distance between patches i, j with spatial coordinates (s_i, t_i) and (s_j, t_j) , respectively. The spatial graph captures immediate tissue-level relationships within the tumor vicinity, such as keratinization, cellular organization patterns, and stromal interactions.

Contextual feature derivation: To derive the contextual patch features (h_n^1) from local patch features (h_n^0), we propose an attention-based graph convolutional network *Att-GNN*. Each convolution layer uses self-attention-based message-passing to propagate feature information from the 1-hop connected nodes j of a node i ($A_{ij} > 0$), updating node features via the following operation:

$$H^{l+1} = GConv(H^l, A; W^l) \quad (4)$$

where $H^l = [h_1^l, h_2^l, \dots, h_N^l]$ and W^l are the trainable parameters of layer l . The adjacency matrix A defines the underlying graph structure, which can be based on either spatial relationships (A^{spa}) or latent similarities (\tilde{A}^{lat}).

To enable relational reasoning over heterogeneous tissue structures, we incorporate self-attention within each graph, leveraging the graph transformer architecture (Hu et al. (2020)). Each graph employs single-head self-attention with a distinct projection head to learn edge weights, enabling patches to prioritize relevant neighbours dynamically. In each graph, node embeddings (target nodes) are projected into key vectors using the projection matrix $W_k \in \mathbf{R}^{d \times d}$. Neighbouring nodes (source nodes) connected to the target node are independently projected into query vectors using the projection matrix $W_q \in \mathbf{R}^{d \times d}$. We use distinct matrices for latent (W_{att}^{lat}) and spatial (W_{att}^{spa}) graphs to capture different semantic relations. The graph edge weights are computed using dot-product attention between each edge's corresponding key and query vectors.

$$\alpha_{ij}^{(l)} = \frac{(h_i^{(l)} W_k^{(l)}) \cdot W_{att}^t \cdot (h_j^{(l)} W_q^t)}{\sqrt{d}}; t \in \{lat, spa\} \quad (5)$$

where d is the dimension of the key and query vectors, i is the central node and j is the neighbouring node. We apply a softmax operation to normalize the attention weights across all neighbours of the source node $j \in \mathcal{N}(i)$:

$$\beta_{ij}^{(l)} = \frac{\exp(\alpha_{ij}^{(l)})}{\sum_{k \in \mathcal{N}(i)} \exp(\alpha_{ik}^{(l)})} \quad (6)$$

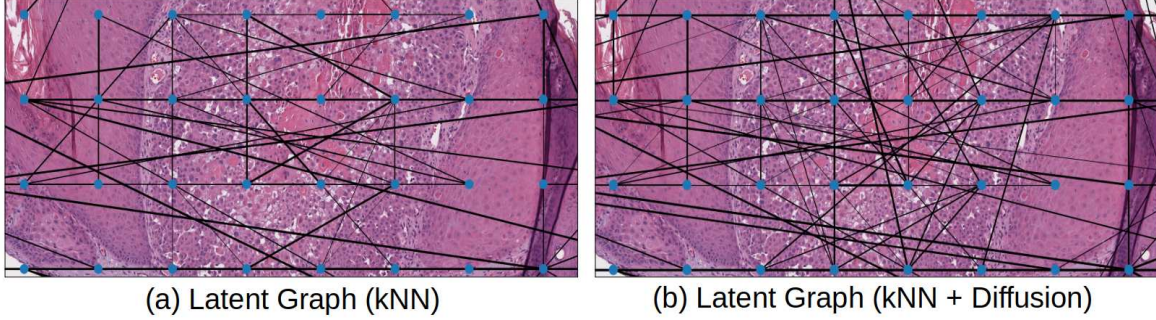


Figure 3: Latent graph refinement using graph diffusion: (a) initial graph defined using 8-nearest neighbours based on feature similarity; (b) refined graph with denser edges. For interpretability, we only highlight the edges with cosine similarity ≥ 0.5

Next, we compute the value vector for each neighboring node using the projection matrix $W_v \in \mathbb{R}^{d \times d}$ and aggregate the value vectors using the normalized attention weights to derive the updated contextual feature for each node:

$$h_i^{n(l+1)} = \sum_{j \in N(i)} \beta_{ij}^{n(l)} (h_j^{(l)} W_v^{(l)}) \quad (7)$$

where β_{ij}^l is the normalized attention weight for each edge. Using separate attention heads allows the model to disentangle spatial and latent features and capture distinct semantic relationships. However, overlapping edges between the spatial and latent graphs can introduce redundancy, particularly under weak supervision. To mitigate this, we introduce a diversity loss that minimizes redundancy by reducing the correlation between the attention weight matrices (W_{att}^{lat} and W_{att}^{spa}). This is achieved using a cosine similarity-based formulation:

$$\mathcal{L}_{diversity} = 1 - \frac{W_{att}^{lat} \cdot W_{att}^{spa}}{\|W_{att}^{lat}\| \|W_{att}^{spa}\|} \quad (8)$$

This cosine similarity-based loss encourages disentanglement, ensuring the spatial and latent graphs focus on complementary relations. This enhances the spatial graph’s ability to encode tumor-specific contexts (e.g., heterogeneity in tumor microenvironment) beyond the phenotypical similarity captured by the latent graph. The contextual patch feature is then computed by averaging the spatial and latent contextual features, followed by a non-linear activation (ReLU) to the aggregated feature. To ensure stable training of the graph network, we apply layer normalization to the aggregated feature, consistent with prior studies (Li et al. (2020)). Given the fine-grained nature of grading, we preserve local patch features using a residual connection (Li et al. (2020)), resulting in the final contextual patch feature h_n^1 :

$$\begin{aligned} h_n^1 &= h_n^0 + \text{ReLU}[\text{norm}(h_{combine}^1)] \\ h_{combine}^1 &= \text{GConv}^{latent}(h_n^0) + \text{GConv}^{spatial}(h_n^0) \end{aligned} \quad (9)$$

3.2. Grade Classification

We use an attention-based aggregation mechanism to determine the contribution of each patch to the overall WSI prediction. Unlike traditional pooling methods, attention can selectively up-weight diagnostically important patches, allowing the model to focus on relevant tumor regions in the presence of tissue heterogeneity. We compute attention weights using the 1-hop contextual node embeddings (h_n^1), obtained from the graph network. Following Ilse et al. (2018), the normalized attention score for each patch x_n is computed using a two-layer network:

$$w_n = \frac{\exp[a^T \tanh(U \cdot h_n^1)]}{\sum_{n \in \Omega_b} \exp[a^T \tanh(U \cdot h_n^1)]} \quad (10)$$

where $a \in \mathbb{R}^d$ and $U \in \mathbb{R}^{d \times d}$ are learnable parameters. Instead of conventional attention pooling over patch-level features, we perform attention-weighted aggregation over patch-level class scores derived using a grade classifier.

This decoupling of patch classification and attention scoring allows RACR-MIL to equally optimize both components, resulting in more robust WSI-level predictions (Early et al. (2024)). We use a cosine softmax classifier to compute patch-level class scores. Specifically, each patch embedding h_n^1 is l_2 -normalized and its dot product with the corresponding class prototype z_c yields the patch-level class-specific logit score:

$$s_{n,c} = \sigma\left(\frac{h_n^1}{\|h_n^1\|} \cdot \frac{z_c}{\tau}\right) \quad (11)$$

where σ is ReLU activation, τ is temperature-scaling hyperparameter, $c \in \{0, 1, 2, 3\}$ representing {normal, well, moderate, poor}, \cdot represents dot product and z_c is defined as the average of normalized patch embeddings assigned to class c , $z_c = \frac{1}{N_c} \sum_{n:y_n=c} \frac{h_n^1}{\|h_n^1\|}$. Normalizing patch features prevents the classifier from relying on feature norms, thereby reducing bias toward dominant, easier-to-classify classes (e.g., well-differentiated tumors in skin SCC) and improving robustness under class imbalance. Moreover, applying ReLU activation over the logits encourages the model to assign higher cosine similarity to the correct class, improving discriminability. Finally, the WSI-level class-likelihood is computed as:

$$p_{b,c} = \sum_{n=1}^N w_n s_{n,c} \quad (12)$$

This formulation improves patch-level class confidence, which is critical for ordinal ranking as well as ensuring that diagnostically relevant patches have higher contribution towards the final WSI prediction. To counter class imbalance due to a lower proportion of poorly differentiated cases, we leverage class-balanced sampling Cui et al. (2019) during training. We use the ground-truth WSI grade label Y_b to compute our MIL-based grade classification loss:

$$\mathcal{L}_{grade} = -\frac{1}{B} \sum_{b=1}^B \sum_c \mathbf{1}(Y_b = c) \log(p_{b,c}) \quad (13)$$

3.2.1. Ordinal Ranking of Patches

We apply two ranking constraints on the attention network to ensure consistent ranking of tumor regions: (i) an inter-grade constraint to impose higher attention values for higher-grade patches, and (ii) an intra-grade constraint to impose higher attention values for more likely patches within the same grade class.

Inter-grade ranking: Pathologists assign greater importance to the most severe tumor regions, implicitly ranking different tumor sections based on their severity. Inspired by this, we introduce an *inter-class ranking constraint* by enforcing pairwise inequality relationships, ensuring that more severe tissue regions are assigned higher scores by the attention network ($w_n^{normal} < w_n^{well} < w_n^{moderate} < w_n^{poor}$). Directly applying this ranking at the patch level is infeasible due to the lack of ground-truth grade annotations for individual patches. To overcome this, we utilize our cosine softmax classifier to estimate a grade confidence score for each patch based on its class likelihoods $p_{n,c}$ learned by the model:

$$p_{n,c} = p(y_n = c | h_n^1) = \frac{\exp[s_{n,c}]}{\sum_{c'} \exp[s_{n,c'}]} \quad (14)$$

These confidence scores allow us to aggregate patch-level features and derive WSI-level class features $W_b^c \in \mathbf{R}^d$, which serve as WSI-specific tumor region prototypes representing specific grades.

$$W_b^c = \sum_{n \in \Omega_b} p_{n,c} \cdot h_n^1 \quad (15)$$

The confidence score $p_{n,c}$ acts as a soft selection mechanism, ensuring that patches contribute to the grade-prototype representation proportionally to their class likelihood. We compute an attention score for each WSI-level class feature, which determines how much focus the model assigns to each tumor region prototype:

$$w_{b,c} = \frac{\exp[a^T \tanh(U \cdot W_b^c)]}{\sum_{c \in \{0,1,2,3\}} \exp[a^T \tanh(U \cdot W_b^c)]} \quad (16)$$

To enforce the clinically relevant prioritization of aggressive tumor areas, we define a set of pairwise prototype comparisons (i, j) between regions corresponding to adjacent grades: $Z = \{(i, j); Y_{b,i} = c, Y_{b,j} = c + 1, c \in \{0, 1, 2\}\}$. We apply a pairwise ranking loss to enforce an ordinal relationship between their attention weights, ensuring that more severe grades are assigned higher attention:

$$\mathcal{L}_{inter} = \sum_{i,j \in Z} \log[1 + \exp(w_{b,i} - w_{b,j})] \quad (17)$$

To enhance the reliability of region prototypes, we select only high-confidence patches for aggregation, including those with a class probability $p_{n,c} > 0.5$. This step minimizes the influence of ambiguous or misclassified patches, ensuring that the learned prototypes reliably represent their respective tumor grades.

Intra-grade ranking: In addition, we impose an *intra-class ranking constraint* to encourage the model to prioritize the most confident patches within each grade class during feature aggregation. Specifically, we construct a candidate patch set by combining the top K patches with the highest attention weights w_n and the top K patches with the highest class probabilities $p_{n,c}$:

$$S = \{n \mid n \in \text{Top}_K(w_n) \cup \text{Top}_K(p_{n,c})\}$$

Within this set, we assign coarse ordinal rankings to class probabilities $p_{n,c}$ by discretizing them into fixed-width bins of size δ . We then construct pairwise ranking constraints between patches whose binned probabilities differ:

$$\tilde{Z} = \left\{ (i, j) \mid \left\lfloor \frac{p_{i,c}}{\delta} \right\rfloor < \left\lfloor \frac{p_{j,c}}{\delta} \right\rfloor; i, j \in S, c \in \{0, 1, 2, 3\} \right\}$$

Using $\delta = 0.1$ allows us to limit the number of pairs due to computational memory constraints. For each pair (i, j) , we apply a RankNet-based ranking loss (Burges et al. (2005)) to align attention weights with the relative class confidence:

$$\mathcal{L}_{intra} = \sum_{(i,j) \in \tilde{Z}} S_{ij} \log \sigma(w_i - w_j) + (1 - S_{ij}) \log(1 - \sigma(w_i - w_j))$$

where $\sigma(\cdot)$ is the sigmoid function, and

$$S_{ij} = \begin{cases} 1 & \text{if } \left\lfloor \frac{p_{j,c}}{\delta} \right\rfloor > \left\lfloor \frac{p_{i,c}}{\delta} \right\rfloor \\ 0 & \text{if } \left\lfloor \frac{p_{j,c}}{\delta} \right\rfloor = \left\lfloor \frac{p_{i,c}}{\delta} \right\rfloor \\ -1 & \text{if } \left\lfloor \frac{p_{j,c}}{\delta} \right\rfloor < \left\lfloor \frac{p_{i,c}}{\delta} \right\rfloor \end{cases}$$

This formulation enforces consistency between the model’s patch-level grade confidence and attention score, encouraging higher importance to more representative grade regions.

Overall Loss: The overall loss combines the grade classification loss, inter-grade and intra-grade attention ranking losses and graph diversity loss. To balance the losses, we used the weighing factors λ_1 and λ_2 , which are determined using hyperparameter tuning:

$$\mathcal{L}_{total} = \mathcal{L}_{grade} + \lambda_1(\mathcal{L}_{inter} + \mathcal{L}_{intra}) + \lambda_2 \mathcal{L}_{diversity} \quad (18)$$

4. Experimental Setup

4.1. Datasets

To validate the effectiveness of our proposed framework, we assess multi-class SCC grading on public and private datasets: two publicly available datasets for lung SCC and head and neck SCC collated from the Cancer Genome Atlas (TCGA) (Tomczak et al. (2015)) and Clinical Proteomic Tumor Analysis Consortium (CPTAC) (Edwards et al. (2015)), along with our own collected histology dataset for skin SCC. Each WSI is associated with a single grade label annotated by pathologists, and no pixel-level annotation was used for training. Table 1 provides a high-level grade distribution for each dataset.

Private Dataset (Skin SCC): We curated a dataset of 815 formalin-fixed paraffin-embedded hematoxylin and eosin (H&E)-stained WSIs, each from a unique patient, collected at the Mayo Clinic, USA. The dataset includes 247 normal, 383 well-differentiated, 108 moderately-differentiated, and 77 poorly-differentiated cases. The majority of patients

were elderly white individuals (mean age: 82 years). WSIs were scanned using an Aperio AT2 scanner at 40X magnification ($0.25\mu\text{m}/\text{pixel}$) between 2017 and 2022. Each slide was independently graded by two expert pathologists based on cellular differentiation, followed by review and confirmation by a supervising dermatologist. In instances of disagreement, the re-reviewing pathologist and dermatologist discussed to arrive at a consensus and excluded cases in which no consensus was achieved. The dataset reflects real-world clinical variability in tissue morphology, slide quality, and class imbalance. A subset of WSIs was annotated at the pixel level to delineate tumor regions for evaluating model localization during inference only.

Public Datasets: To highlight the strong performance of our model across diverse SCC tumors, we utilized the publicly available cancer datasets from TCGA and CPTAC.

Lung SCC: For lung cancer, we use 289 diagnostic FFPE H&E WSIs from the CPTAC-LSCC study, representing 109 patients. The dataset comprises 161 normal, 72 moderately-differentiated, and 56 poorly-differentiated cases. Due to the lack of well-differentiated tumors, lung SCC grading was formulated as a 3-class classification task. All WSIs were scanned at 40X magnification ($0.25\mu\text{m}/\text{pixel}$), and grade labels were assigned at the patient level.

Head and Neck SCC: The head and neck SCC dataset is assembled from 310 WSIs from TCGA-HNSC and 362 WSIs from CPTAC-HNSCC, totaling 672 patient cases. It includes 105 normal, 79 well-differentiated, 356 moderately-differentiated, and 132 poorly-differentiated tumors. All diagnostic WSIs for each patient were included in the analysis. To address the scarcity of well-differentiated samples in individual datasets and leverage normal WSIs available in CPTAC-HNSCC, both sources were merged. All WSIs were scanned at 40X magnification ($0.25\mu\text{m}/\text{pixel}$). For TCGA-HNSC, grade labels were derived from pathology reports available via cBioPortal (Gao et al. (2013)).

Dataset	Source	Usage	Normal	Well	Mod	Poor	Total
Skin	Private	Train, Test	247	383	108	77	815
Lung	CPTAC	Train, Test	161	-	72	56	289
Head & Neck	CPTAC, TCGA	Train, Test	105	79	356	132	672

Table 1: Data distribution of the datasets

4.2. Pathologists Review

We assess our trained model to determine its effectiveness in improving pathologists’ performance in diagnosing skin SCC tumor grades. Two board-certified pathologists analyzed 12 WSIs, each diagnosing 6 cases with and without model assistance, separated by a cooling period of three months between diagnoses. During diagnosis, pathologists reviewed the WSI with tumor-grade heatmaps overlaid on the image. They were required to provide feedback on the impact of model assistance, focusing on the localization of grade-relevant tumor regions, identification of false positives and false negatives, and the model’s impact on diagnosis efficiency.

4.3. Tissue Extraction

We preprocess each WSI using thresholding and morphological operations to remove background regions and irrelevant tissue sections (area below 20). Each tissue region was downsampled to 20X magnification and Otsu thresholding was used to extract relevant tissue regions. We tile each WSI into non-overlapping 448×448 patches and remove patches with minimal texture using image gradient-based entropy with a threshold of 4.

4.4. Training Details

We use the Nest-S encoder Zhang et al. (2022) for self-supervised pretraining using the DINO framework, learning separate feature extractors for each SCC dataset. RACR-MIL was then trained to classify WSIs into four classes (Normal, Well-, Moderately-, and Poorly-differentiated) for skin SCC and head & neck SCC, and three classes (Normal, Moderately-, and Poorly-differentiated) for lung SCC. The graph-based feature extractor and grade classifier were jointly optimized using AdamW (batch size 16). We report the set of optimal hyperparameters leading to the best test accuracy for RACR-MIL in the appendix (Table A.5). Model evaluation was conducted using 5-fold cross-validation with a 64:16:20 train/validation/test split, stratified to address class imbalance. We use seven different evaluation metrics averaged over the folds to assess the model’s performance: macro-averaged Precision, Recall and F1 score; quadratic-weighted κ ; class-wise accuracy; Area Under Curve (AUC) for low- vs high-risk (well- vs moderate/poor) grades; and Matthews Correlation Coefficient (MCC).

Table 2: Comparison of RACR-MIL with state-of-the-art MIL approaches for SCC grading using DINO-pretrained feature extractor. For each evaluation metric, the mean and standard deviation across five cross-validation folds are reported. **Bold** and Underline indicate the highest and second highest performance.

Approach	Skin SCC					Head & Neck SCC					Lung SCC				
	F1	Precision	Recall	AUC	MCC	F1	Precision	Recall	AUC	MCC	F1	Precision	Recall	AUC	MCC
Non-contextual															
Max Pooling	0.761 _{0.039}	0.770 _{0.040}	0.776 _{0.044}	0.942 _{0.011}	0.762 _{0.053}	0.561 _{0.017}	0.554 _{0.018}	0.583 _{0.034}	0.810 _{0.035}	0.395 _{0.062}	0.699 _{0.047}	0.714 _{0.050}	0.717 _{0.042}	0.919 _{0.020}	0.670 _{0.058}
Mean Pooling	0.758 _{0.027}	0.756 _{0.030}	0.771 _{0.030}	0.943 _{0.014}	0.754 _{0.041}	0.590 _{0.010}	0.581 _{0.032}	0.621 _{0.036}	0.818 _{0.026}	0.419 _{0.053}	<u>0.742</u> _{0.064}	<u>0.745</u> _{0.067}	<u>0.751</u> _{0.067}	<u>0.936</u> _{0.028}	<u>0.716</u> _{0.077}
ABMIL	0.782 _{0.027}	0.774 _{0.035}	<u>0.805</u> _{0.022}	<u>0.954</u> _{0.009}	<u>0.781</u> _{0.042}	<u>0.604</u> _{0.014}	<u>0.596</u> _{0.039}	0.623 _{0.033}	0.830 _{0.022}	<u>0.445</u> _{0.051}	0.690 _{0.035}	0.709 _{0.044}	0.713 _{0.059}	0.930 _{0.025}	0.664 _{0.060}
GABMIL	0.770 _{0.021}	0.770 _{0.026}	0.787 _{0.017}	0.957 _{0.010}	0.780 _{0.020}	0.585 _{0.010}	0.574 _{0.050}	0.606 _{0.056}	0.821 _{0.027}	0.415 _{0.079}	0.702 _{0.060}	0.708 _{0.065}	0.713 _{0.067}	0.933 _{0.023}	0.671 _{0.075}
CLAM-MB	0.778 _{0.024}	<u>0.775</u> _{0.030}	0.789 _{0.017}	<u>0.954</u> _{0.011}	<u>0.781</u> _{0.030}	0.600 _{0.014}	0.591 _{0.039}	0.620 _{0.033}	0.813 _{0.022}	0.435 _{0.051}	0.707 _{0.047}	0.715 _{0.048}	0.722 _{0.054}	0.932 _{0.024}	0.681 _{0.064}
Contextual															
PatchGCN	0.772 _{0.019}	0.762 _{0.023}	0.799 _{0.027}	0.950 _{0.010}	0.766 _{0.042}	0.582 _{0.024}	0.577 _{0.019}	0.597 _{0.035}	0.815 _{0.026}	0.415 _{0.044}	0.689 _{0.053}	0.703 _{0.059}	0.709 _{0.064}	0.934 _{0.019}	0.660 _{0.085}
WiKG	0.763 _{0.007}	0.770 _{0.014}	0.772 _{0.017}	0.940 _{0.011}	0.768 _{0.039}	0.586 _{0.019}	0.592 _{0.034}	0.600 _{0.044}	0.800 _{0.032}	0.432 _{0.050}	0.702 _{0.071}	0.707 _{0.069}	0.707 _{0.079}	0.906 _{0.032}	0.666 _{0.085}
TransMIL	0.718 _{0.041}	0.728 _{0.047}	0.731 _{0.047}	0.919 _{0.015}	0.727 _{0.040}	0.555 _{0.007}	0.549 _{0.009}	0.593 _{0.015}	0.806 _{0.025}	0.383 _{0.037}	0.696 _{0.072}	0.712 _{0.069}	0.703 _{0.076}	0.927 _{0.028}	0.669 _{0.074}
GTP	0.728 _{0.034}	0.737 _{0.042}	0.732 _{0.035}	0.934 _{0.019}	0.725 _{0.036}	0.541 _{0.019}	0.538 _{0.041}	0.574 _{0.041}	0.791 _{0.061}	0.378 _{0.061}	0.694 _{0.060}	0.701 _{0.064}	0.697 _{0.075}	0.918 _{0.027}	0.657 _{0.084}
DSMIL	0.761 _{0.042}	0.762 _{0.038}	0.774 _{0.032}	0.950 _{0.015}	0.770 _{0.040}	0.565 _{0.011}	0.558 _{0.048}	0.594 _{0.068}	0.812 _{0.031}	0.379 _{0.083}	0.676 _{0.057}	0.689 _{0.059}	0.699 _{0.056}	0.929 _{0.020}	0.663 _{0.072}
RACR-MIL	0.807 _{0.013}	0.796 _{0.019}	0.831 _{0.028}	0.958 _{0.007}	0.801 _{0.027}	0.615 _{0.016}	0.608 _{0.017}	0.643 _{0.049}	<u>0.827</u> _{0.024}	0.452 _{0.064}	0.745 _{0.049}	0.752 _{0.043}	0.758 _{0.049}	0.939 _{0.021}	0.717 _{0.063}

4.5. Baselines

We compare our framework against state-of-the-art attention-based MIL models, grouped into two categories: 1) non-contextual methods that treat patches independently, including ABMIL (Ilse et al. (2018)), Gated ABMIL (Ilse et al. (2018)), CLAM-MB (Lu et al. (2021)), Mean Pooling and Max Pooling; 2) contextual methods that account for patch dependencies, including PatchGCN (Chen et al. (2021)), DSMIL (Li et al. (2021)), TransMIL (Shao et al. (2021)), WiKG (Li et al. (2024)) and Graph Transformer (GTP) (Zheng et al. (2022)). All baselines, except Mean Pooling and Max Pooling, leverage attention-based feature pooling. CLAM-MB builds on ABMIL, focusing on individual patch features and incorporates a clustering layer to enhance discriminability. PatchGCN uses a spatial graph and spectral graph convolution, while WiKG learns separate head and tail embeddings using a directed spatial graph with a knowledge-aware attention mechanism. TransMIL uses a transformer to model short- and long-range patch dependencies and GTP combines graph-based patch feature representation with transformer for feature aggregation. DSMIL uses dual classifiers at the bag and instance levels and leverages self-attention to model patch interaction.

Additionally, we compare variants of our RACR model - incorporating only subsets of proposed innovations (e.g., spatial or latent contextual features, attention ranking) - to evaluate their contributions to classification performance. We also evaluate the tumor localization capability of our approach on the skin SCC dataset. For a fair comparison, all approaches use the same pre-trained feature extractor. Baseline hyperparameters (e.g., learning rate, dropout rate, number of layers, embedding dimension) were fine-tuned to optimize performance on each SCC dataset. We keep the batch size and Adam optimizer’s weight decay consistent across methods to ensure a fair comparison.

5. Results

5.1. Grade Classification

5.1.1. Enhanced grading performance on skin SCC

We first evaluate RACR-MIL on the internal skin SCC dataset and observe consistent improvements over state-of-the-art attention models across all evaluation metrics (Table 2). RACR-MIL outperforms non-contextual methods with 3-5% higher F1 and 2-5% higher MCC scores. Compared to contextual methods, our method achieves 4-9% higher F1 and 4-8% higher MCC scores. Our model achieves significant performance improvement over TransMIL and GTP, which rely on transformer architecture and full pairwise attention, underscoring the value of explicitly encoding semantic relationships between patches using graphs. Moreover, compared to DSMIL and PatchGCN, which incorporate either latent dependency or spatial dependency, our joint modeling approach achieves a 4-5% higher F1 score. Consistent with prior findings in weakly-supervised grading (Dominguez-Morales et al. (2024)), we observe that ABMIL serves as a strong baseline, outperforming existing contextual methods except for RACR-MIL. Our model’s improved performance highlights that explicit modeling of tissue dependencies along with consistent prioritization of relevant regions, can enable contextual methods to surpass non-contextual approaches. While larger 448×448 patches can partially compensate for limited context in our case, broader tissue context is important for maximizing grading performance under weak supervision. RACR-MIL also exhibits lower standard deviation across all metrics, underscoring its robustness and generalizability across diverse evaluation cohorts.

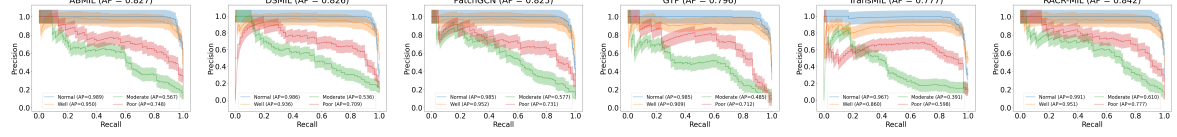


Figure 4: Precision-recall curves for skin SCC: RACR-MIL achieves the highest average precision across all grades, highlighting its robustness.

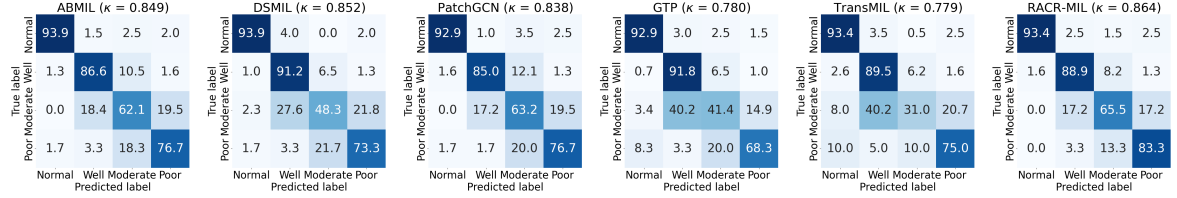


Figure 5: Confusion matrices for skin SCC: RACR-MIL achieves highest κ score and classification accuracy on challenging worse-grade tumors.

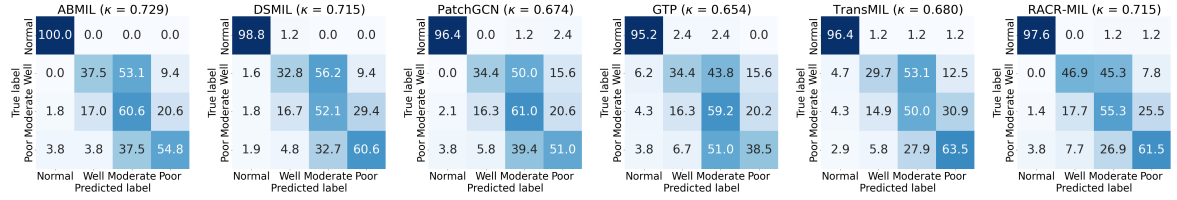


Figure 6: Confusion matrices for head and neck SCC: RACR-MIL achieves balanced performance across grades with highest κ score across contextual approaches.

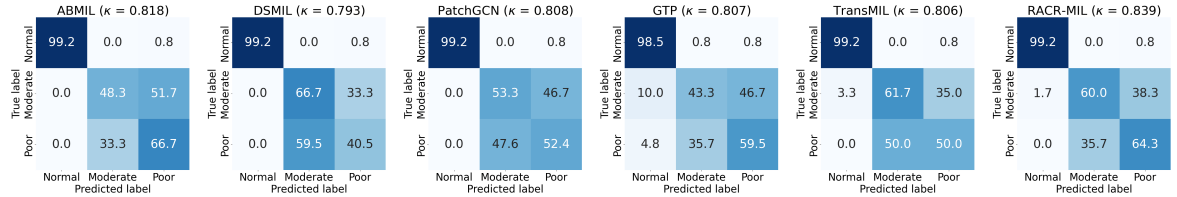


Figure 7: Confusion matrices for lung SCC: RACR-MIL achieves highest κ score outperforming all approaches on Poorly-differentiated tumors.

5.1.2. Generalizability across diverse SCCs

In addition to skin, RACR-MIL demonstrates superior grading performance across two other anatomies - head & neck SCC and lung SCC, as shown in Table 2. On head and neck SCC, RACR-MIL achieves the highest F1 score and MCC, showing competitive performance across all metrics. It outperforms contextual baselines by 4-7% in F1 and 2-5% in MCC, underscoring its improved ability to learn grade-relevant contextual features. In lung SCC, our approach outperforms all baselines, achieving more than 4% improvement in F1 and MCC scores compared to contextual methods. Moreover, RACR-MIL demonstrates lower standard deviation across all metrics compared to the majority of the baselines. Our model’s balanced precision and recall scores (0.752 vs 0.758) highlight its effectiveness in minimizing false positives while maintaining high sensitivity on lung SCC.

5.1.3. Class-wise Performance

The performance on each grade class for RACR-MIL and baseline models on skin SCC dataset is shown in Figures 4 and 5. Our model consistently outperforms baselines across all tumor grades, achieving an average precision of 0.842 and κ score of 0.864, improving over existing contextual methods by up-to 8%. In particular, RACR-MIL achieves the highest accuracy for higher-risk moderate- and poorly-differentiated cases, with improvements of up

Table 3: Localization accuracy of RACR-MIL vs ABMIL for clinically relevant tumor regions identified by three expert pathologists (skin SCC)

Approach	Pathologist 1				Pathologist 2				Pathologist 3			
	Correct Grade		Incorrect Grade		Correct Grade		Incorrect Grade		Correct Grade		Incorrect Grade	
	Sensitivity	Saliency	Sensitivity	Saliency	Sensitivity	Saliency	Sensitivity	Saliency	Sensitivity	Saliency	Sensitivity	Saliency
ABMIL	0.663	0.589	0.647	0.472	0.642	0.582	0.548	0.534	0.763	0.655	0.786	0.672
RACR-MIL	0.682	0.601	0.780	0.531	0.797	0.678	0.578	0.470	0.797	0.671	0.797	0.572

to 28% and 15% over baselines, respectively. By incorporating ranking and cosine-softmax classifier, our approach remains robust to class imbalance, enhancing performance on the minority worse-grade classes while maintaining comparable accuracy on the dominant well-differentiated class. We also observe that transformer-based contextual methods tend to overfit on the dominant class at the expense of minority classes. Graph-based methods such as PatchGCN and RACR-MIL achieve a more balanced performance, with our approach demonstrating superior overall results due to the improved hybrid dual graph formulation.

Figure 6 highlights the class-wise performance of RACR-MIL and baseline methods on head & neck SCC. While RACR-MIL has a lower accuracy on the dominant ‘Moderate’ class (53% cases), it is robust to class imbalance and achieves a balanced performance across moderately- and poorly-differentiated cases. In contrast, existing contextual methods tend to overfit to the dominant classes, leading to lower κ scores. Our model outperforms DSMIL on the more challenging worse-grade tumors while achieving a comparable κ score. In comparison to ABMIL, RACR-MIL is less prone to overfitting and significantly improves on the minority well-differentiated class (12% cases). RACR-MIL’s robustness is also supported by higher average precision compared to existing contextual methods, as shown in Figure A.13 (appendix).

On lung SCC (Figure 7), RACR-MIL achieves the highest κ score as well as grading accuracy on poorly-differentiated tumors compared to contextual methods. It significantly outperforms the next best approach (PatchGCN) by more than 7% on worse-grade tumors. Our approach’s balanced performance across higher-risk tumors and highest average precision across tumor classes further underscores its robustness (Figure A.14 in the appendix). We also observe that across skin and lung SCCs, ours is the only contextual approach that outperforms ABMIL on κ score, achieving better accuracy on the challenging Moderately-differentiated cases.

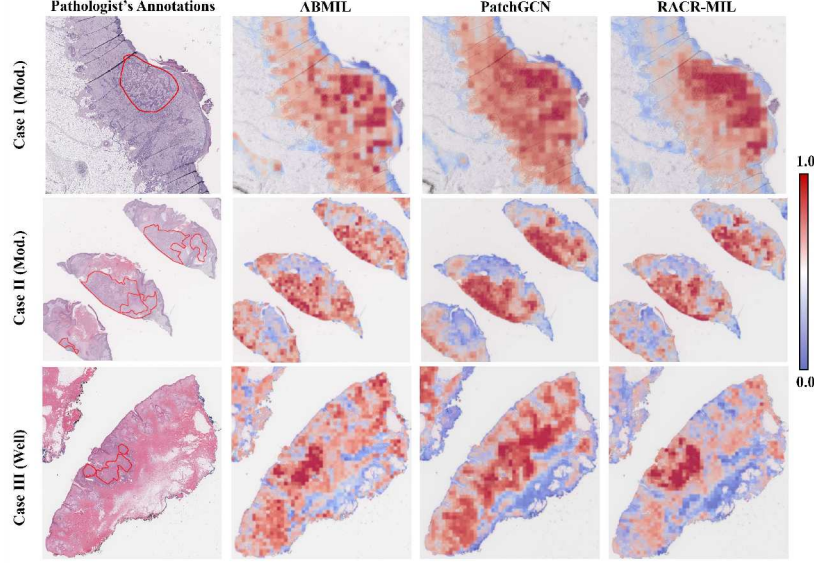
5.2. Tumor Localization

We evaluate the localization ability of RACR-MIL through qualitative visual inspection and quantitative analysis. In line with the experimental design of Tourniaire et al. (2024), we compute the region-level overlap to quantify RACR-MIL’s ability to localize relevant tumor regions annotated by pathologists.

5.2.1. Improved coverage of relevant tumor regions

A random sample of 19 WSIs was chosen for review and annotation by three senior pathologists comprising 5 well-, 6 moderately-, and 8 poorly-differentiated cases. A test set was created using these WSIs while the remaining WSIs were leveraged for training RACR-MIL using the optimal hyperparameters described in the appendix (Table A.5). Each pathologist analyzed all of the 19 cases and identified up to 7 tumor regions per WSI that were most relevant for grade determination. Each region’s grade label was determined according to its dominant histologic feature. The annotations were then used to determine the extent of overlap with the model’s top-identified regions of interest (ROIs). The ROIs were identified based on the predicted grade probability for each patch ($p_{n,c}$). Following the disease localization protocol proposed by Sun et al. (2025), we define the model ROIs as top 25% patches with the highest attention scores having grade-class probability more than 50%. Given the inherent limitations of the pathologist annotations, which may not exhaustively delineate all tumor areas, we employ ‘sensitivity’ as a primary metric to assess the model’s ability to localize critical tumor regions. Sensitivity is defined as the proportion of annotated regions overlapping with the model’s ROIs. We further categorize annotations into *Correct Grade* and *Incorrect Grade* groups based on whether the model accurately predicted each region’s grade. To assess the model’s robustness, we also compute ‘saliency’ as the average model confidence (predicted class probability) for each annotated region. Both metrics were averaged group-wise across tumor regions. As shown in Table 3, RACR-MIL consistently demonstrates higher sensitivity compared to ABMIL across all pathologists, indicating improved coverage of relevant tumor regions. Furthermore, RACR-MIL exhibits higher saliency, particularly for correctly classified regions, suggesting more confident and reliable predictions when the model is accurate.

Figure 8: Normalized attention heatmaps highlighting the tumor ROIs prioritized by different models. Patch-level tumor grade annotations are highlighted with a 'Red' outline in the leftmost panel. In the heatmaps, 'Red' and Blue indicate high and low attention regions, respectively.



5.2.2. Improved alignment with pathologist's annotations

We highlight the impact of the proposed innovations on tumor localization by analyzing the normalized attention heatmaps of three WSIs (Figure 8). The heatmaps were derived by scaling the attention weight w_n for each patch across the corresponding WSI ($a_n = (w_n - w_n^{min}) / (w_n^{max} - w_n^{min})$). Our model localizes the important tumor regions accurately, achieving higher consistency with the pathologists' annotations. In Cases I and II, leveraging dual graphs allows RACR-MIL to capture a larger portion of the tumor without suffering from oversmoothing. In Case III, leveraging the graph and ranking leads to fewer false positives, with higher importance being assigned to the tumor region compared to normal tissue. The heatmaps highlight the importance of incorporating contextual information, as the non-contextual ABMIL approach either assigns similar importance to connective tissue and tumor (Case III) or overlooks key sub-regions within the tumor area (Cases I and II). PatchGCN suffers from oversmoothing and fails to capture fine-grained local context, leading to diffused attention and failure to identify localized tumors accurately (Case III).

5.3. Ablation Study

All innovations in our framework contribute to improvement in grade classification. We experimented with seven variants of our model: 1) graph variants without rank-constrained attention: latent graph only (G_{lat}), spatial graph only (G_{spa}), latent + spatial graphs (G_{dual}); 2) graph variants with ranking constraints: $G_{lat} + \mathcal{L}_{rank}$, $G_{spa} + \mathcal{L}_{rank}$, $G_{dual} + \mathcal{L}_{rank}$; 3) graph variant with ranking constraints and diversity regularization: $G_{dual} + \mathcal{L}_{rank} + \mathcal{L}_{div}$. All seven variants used a cosine-softmax classifier. We also compare variants of our model using the vanilla softmax classifier (G_{dual}^{soft}) with the cosine-softmax classifier (G_{dual}). We observe that the highest gain in F1-score is observed using our dual-graph formulation in conjunction with rank-ordering and diversity regularization.

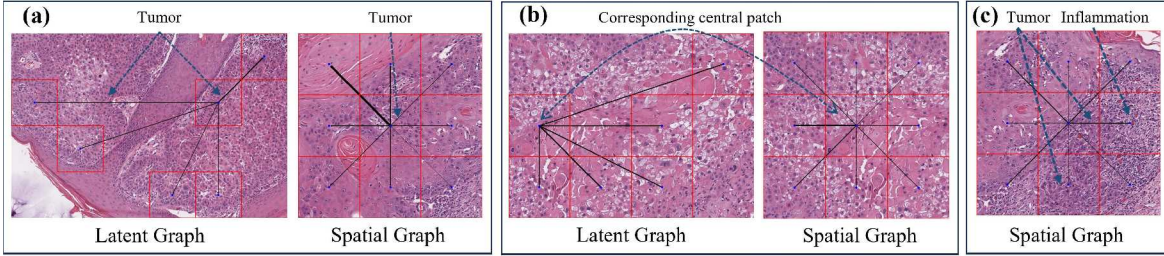
5.3.1. Spatial vs Latent Dependency

We find that combining spatial and latent graphs consistently outperforms using either graph alone, with or without the ranking constraints (Table 4). The dual graph formulation leads to a 1-3% improvement in F1-score across all SCCs and outperforms ABMIL, a strong baseline. Incorporating diversity-based regularization along with the dual graphs further improves classification performance with 3% increase in accuracy for moderately- and poorly-differentiated classes (Figure A.15 in the appendix). We also visualize the latent and spatial graphs learnt by RACR-

Table 4: Impact of ranking ordering constraint, latent encoding and spatial neighbourhood contextual information for patch context aggregation. Leveraging ranking constraint increases F1-score by 2-3% across all SCCs. Integrating latent information with the spatial graph improves the F1-score by 1-2%.

Approach	Skin SCC					Head & Neck SCC					Lung SCC				
	F1	Precision	Recall	AUC	MCC	F1	Precision	Recall	AUC	MCC	F1	Precision	Recall	AUC	MCC
ABMIL	0.782 _{0.027}	0.774 _{0.035}	0.805 _{0.012}	0.954 _{0.009}	0.781 _{0.042}	0.604 _{0.034}	0.596 _{0.039}	0.623 _{0.033}	0.830 _{0.022}	0.445 _{0.051}	0.690 _{0.035}	0.709 _{0.044}	0.713 _{0.039}	0.930 _{0.025}	0.664 _{0.060}
ABMIL + \mathcal{L}_{rank}	0.792 _{0.037}	0.786 _{0.043}	0.809 _{0.026}	0.956 _{0.007}	0.796 _{0.050}	0.606 _{0.051}	0.596 _{0.050}	0.628 _{0.039}	0.818 _{0.032}	0.444 _{0.080}	0.713 _{0.037}	0.729 _{0.047}	0.736 _{0.039}	0.935 _{0.024}	0.686 _{0.058}
RACR-MIL															
G_{lat}	0.790 _{0.014}	0.783 _{0.019}	0.811 _{0.013}	0.962 _{0.006}	0.795 _{0.030}	0.576 _{0.024}	0.572 _{0.022}	0.591 _{0.024}	0.819 _{0.017}	0.414 _{0.053}	0.709 _{0.039}	0.723 _{0.046}	0.724 _{0.043}	0.928 _{0.023}	0.670 _{0.047}
$G_{lat} + \mathcal{L}_{rank}$	0.794 _{0.020}	0.786 _{0.025}	0.812 _{0.011}	0.961 _{0.006}	0.797 _{0.028}	0.588 _{0.023}	0.582 _{0.019}	0.609 _{0.040}	0.817 _{0.024}	0.417 _{0.043}	0.706 _{0.041}	0.727 _{0.033}	0.733 _{0.049}	0.921 _{0.026}	0.677 _{0.060}
G_{spa}	0.769 _{0.021}	0.769 _{0.023}	0.784 _{0.017}	0.957 _{0.010}	0.782 _{0.027}	0.592 _{0.037}	0.584 _{0.038}	0.608 _{0.037}	0.821 _{0.021}	0.427 _{0.069}	0.704 _{0.027}	0.717 _{0.026}	0.719 _{0.038}	0.923 _{0.022}	0.667 _{0.048}
$G_{spa} + \mathcal{L}_{rank}$	0.781 _{0.029}	0.783 _{0.035}	0.791 _{0.016}	0.955 _{0.011}	0.792 _{0.039}	0.595 _{0.045}	0.588 _{0.041}	0.620 _{0.057}	0.818 _{0.023}	0.427 _{0.058}	0.716 _{0.028}	0.732 _{0.041}	0.740 _{0.063}	0.913 _{0.028}	0.686 _{0.073}
$G_{dual} + \mathcal{L}_{div}$	0.793 _{0.023}	0.785 _{0.029}	0.811 _{0.019}	0.955 _{0.009}	0.793 _{0.024}	0.606 _{0.042}	0.597 _{0.044}	0.623 _{0.046}	0.820 _{0.029}	0.437 _{0.055}	0.718 _{0.045}	0.730 _{0.044}	0.735 _{0.053}	0.928 _{0.021}	0.695 _{0.064}
$G_{dual} + \mathcal{L}_{rank}$	0.800 _{0.026}	0.791 _{0.032}	0.817 _{0.016}	0.958 _{0.007}	0.797 _{0.034}	0.611 _{0.036}	0.605 _{0.035}	0.628 _{0.043}	0.823 _{0.029}	0.439 _{0.055}	0.726 _{0.041}	0.735 _{0.044}	0.741 _{0.052}	0.936 _{0.023}	0.696 _{0.054}
$G_{dual}^{off} + \mathcal{L}_{rank} + \mathcal{L}_{div}$	0.792 _{0.034}	0.786 _{0.044}	0.807 _{0.023}	0.951 _{0.008}	0.787 _{0.037}	0.615 _{0.046}	0.608 _{0.037}	0.643 _{0.049}	<u>0.827</u> _{0.024}	0.452 _{0.064}	0.715 _{0.032}	0.721 _{0.050}	0.927 _{0.022}	0.670 _{0.051}	
$G_{dual} + \mathcal{L}_{rank} + \mathcal{L}_{div}$	0.807 _{0.013}	0.796 _{0.019}	0.831 _{0.020}	0.958 _{0.007}	0.801 _{0.027}	0.590 _{0.049}	0.583 _{0.049}	0.613 _{0.038}	0.822 _{0.031}	0.413 _{0.074}	0.745 _{0.036}	0.752 _{0.053}	0.758 _{0.039}	0.939 _{0.021}	0.717 _{0.063}

Figure 9: Contextual relationships learnt by RACR-MIL: (a) Latent graph edge weights emphasize morphologically similar tumor regions and spatial graph assigns higher importance to peri-tumoral features such as keratinization; (b) Distinct edge weight distribution across the latent and spatial graphs enhances RACR-MIL’s ability to capture heterogeneous contextual cues; (c) Spatial graph selectively emphasizes inflammation-associated regions surrounding the central tumor region.



MIL. In Figure 9A, our model focuses on tissue semantics, capturing dependencies between tumor regions and other tissue structures. The latent graph assigns slightly higher importance to nearby tumor regions while capturing contextual information from distant tumor areas. The spatial graph encodes heterogeneous context, such as the presence of keratin near tumor regions, by assigning higher attention edge weight. In Figure 9B, the diversity constraint and distinct edges between the two graphs encourage them to focus on differing context around a patch: the latent graph focuses on stromal tissue with keratin, while the spatial graph assigns higher importance to the tumor with eosinophilic cytoplasm. Additionally, Figure 9C shows that self-attention selectively emphasizes the tumor-inflammation connection in the spatial graph while de-emphasizing the nearby tumor patch, thus capturing microenvironment heterogeneity.

5.3.2. Ranking Constraints

Using the rank-ordering constraints allows RACR-MIL to address tumor heterogeneity by consistently assigning higher attention to higher-grade tumor regions. We find that imposing the ranking constraints improves the F1-score for all graph variants by upto 1.2% (Table 4). The ranking constraints lead to higher accuracy in classifying higher-risk tumors (Figure A.15 in the appendix). We compare the attention heatmaps of ABMIL without ranking constraints with RACR-MIL in Figure 10. In Case I, our model with graph and ranking constraints emphasizes the accurate tumor region (moderately-differentiated) compared to the well-differentiated areas. In Case II, it assigns greater attention to poorly-differentiated regions across all WSI sections. By emphasizing the worst-grade tumor regions during feature pooling, our rank constraint enables RACR-MIL to concentrate on relevant patches aligning with the grade label. Moreover, capturing short- and long-range context allows the model to assign consistent features to patches within tumor regions of interest. Consequently, the model can identify tumors with higher confidence, as evident by the increased class likelihood ($p_{n,c}$) in WSI heatmaps across different grades (Figure 11). This enables the model to delineate a broader tumor section in comparison to ABMIL.

Figure 10: Attention heatmaps highlighting the impact of ranking constraint in assigning consistent importance to tumor regions with different grades (Pathologist Annotations - Red: Poorly-differentiated, Blue: Moderately-differentiated, Green: Well-differentiated)

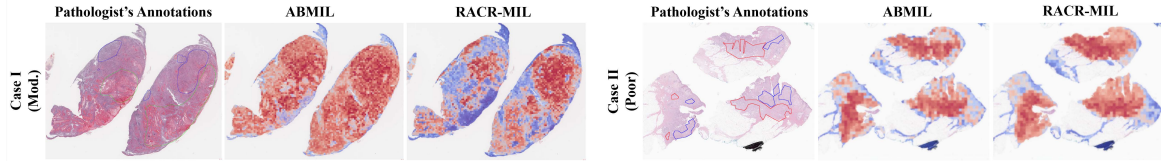
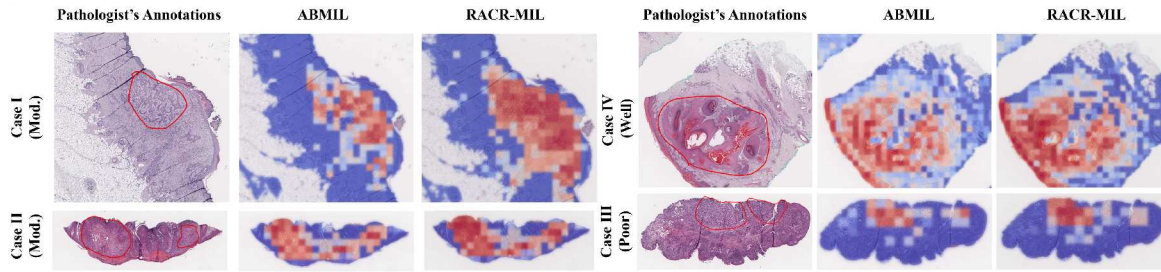


Figure 11: Probability heatmaps illustrating the class likelihood of tumor ROIs identified by our model. Tumor annotations are outlined with a 'Red' boundary in the leftmost panels. In the heatmaps, 'Red' and 'Blue' indicate higher and lower likelihood, respectively. 'Mod.' represents Moderately-differentiated



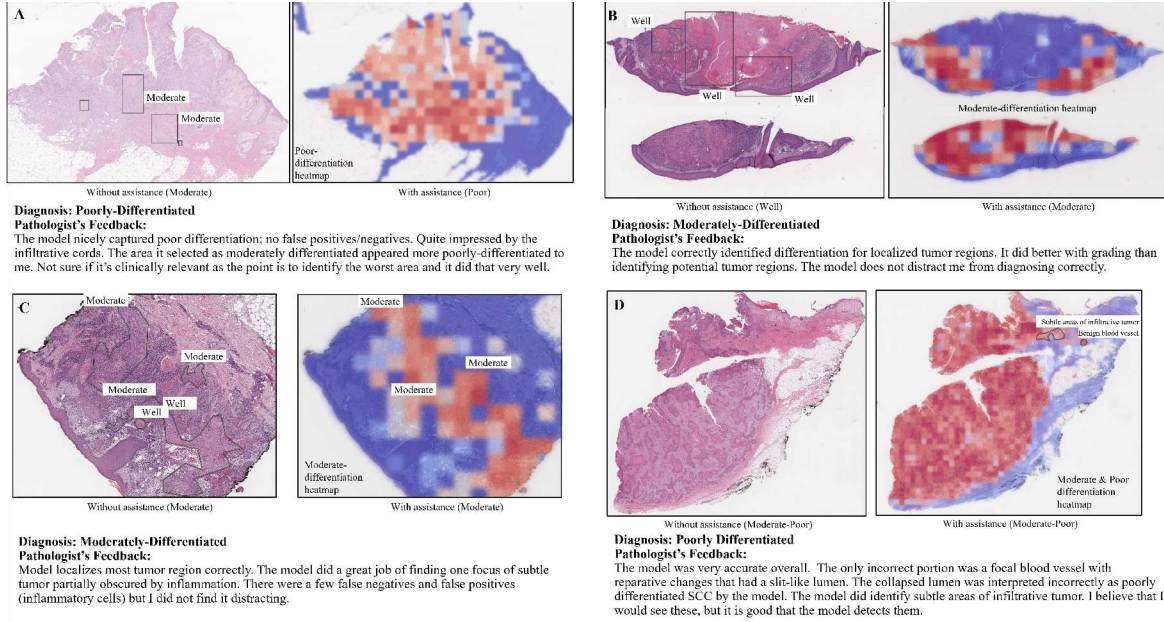
5.4. Evaluating efficacy as a diagnostic assistant

We evaluate RACR-MIL's effectiveness as a diagnostic tool using a small-scale pilot study with two pathologists. We examined the model's impact on pathologists' grading accuracy and its ability to guide them to diagnostically relevant tumor regions. Qualitative feedback from pathologists indicates that the model accurately identified tumor regions and correctly localized the worst-grade tumor ROI(s) in 11 out of 12 cases. The model enhanced diagnostic accuracy across WSIs with small and large-scale tumor regions and successfully highlighted subtle infiltrative patterns, including nuclear atypia. Model assistance led to diagnostic revision in multiple cases, with one pathologist upgrading their grade diagnosis in 3 out of 6 reviewed slides. Representative examples in which the model improved pathologists' accuracy are shown in Figure 12 (A, B). In both these cases, RACR-MIL correctly highlights higher-grade tumor foci, prompting the pathologist to update their diagnosis. In Figure 12B, it delineates moderately-differentiated regions surrounding a well-differentiated tumor that were initially overlooked. In Figures 12C and 12D, the model identified subtle discriminative features such as nuclear atypia dominated by inflammatory cells and infiltrative patterns at the tumor's edge. Overall, pathologists reported that the model improved diagnostic efficiency in 7 out of 12 cases, while in 2 cases the model's output was considered distracting. These findings demonstrate the model's potential for translation as an AI-assisted tool to support more accurate and efficient SCC grading.

6. Conclusion

We present RACR-MIL, a novel multiple instance learning framework for weakly-supervised SCC tumor grading in whole slide images that integrates graph-based contextual learning with rank-ordering constrained pooling. Drawing on clinical domain knowledge, RACR-MIL employs a dual-graph formulation to capture multi-level tissue context: (1) local tumor microenvironment, including relevant non-tumor cues such as keratinization, and (2) phenotypically similar tumor regions, whether spatially close or distant, to reflect tumor growth structure. By leveraging distinct spatial and latent graphs and incorporating self-attention and diversity regularization, our model enhances the extraction of complementary contextual information. RACR-MIL consistently outperforms existing methods across multiple anatomies, with strong improvements in identifying high-risk tumors as well as tumor localization. Each of

Figure 12: Model-guided diagnosis and expert feedback using RACR-MIL for skin SCC: (A, B) RACR-MIL highlighted higher-grade tumor regions missed initially, leading to diagnostic revision. (C, D) The model accurately localized pathologist-annotated regions and identified subtle infiltrative components. Heatmap indicates predicted class likelihood of the diagnosed grade ('Red' and 'Blue' indicate high and low probabilities, respectively).



our proposed innovations consistently improves grading performance, as validated through comprehensive ablation studies. Beyond grading, RACR-MIL's ranking-guided approach can be extended to outcome prediction tasks involving ordinal target, such as tumor burden estimation or survival analysis. Additionally, its accurate identification of diagnostically relevant tumor regions as well as positive clinician feedback in a pilot study highlights its potential as an AI-assisted tool to support and enhance pathologists' workflow.

There are several limitations of this study, that we will address in future work. (i) The model can confuse non-tumor patches with tumor patches, resulting in false positives. Improved feature and contextual information extraction might help in separating different cell types in the feature space. (ii) Our attention network is not optimized for tumor segmentation which might affect the accuracy of tumor localization. Incorporating object detection along with exploring a spatial auxiliary task such as depth prediction might allow the model to capture tumor boundaries better as well as improve grading. (iii) Clinical translation of the proposed method requires quantification of the uncertainty associated with the prediction to build trust. (iv) Finally, the clinical utility of the proposed approach in reducing inter-pathologist variability needs to be evaluated on a larger cohort. Our future work would also focus on extending and evaluating the performance of RACR-MIL's generalizable framework to other cancer sub-types (e.g., adenocarcinoma).

7. CRediT authorship contribution statement

Anirudh Choudhary: Conceptualization, Methodology, Software, Validation, Formal analysis, Investigation, Data curation, Writing – original draft, Writing – review & editing, Visualization. **Mosbah Aouad:** Writing – review & editing, Validation. **Krishnakant Saboo:** Writing - original draft, Validation. **Angelina Hwang:** Data curation, Resources. **Jacob Kechter:** Data curation, Resources. **Blake Bordeaux:** Data curation, Validation. **Puneet Bhullar:** Data curation, Resources. **David DiCaudo:** Validation, Investigation, Data curation. **Steven Nelson:** Validation,

Investigation, Data Curation. **Nneka Comfere**: Validation, Data curation. **Emma Johnson**: Validation, Data curation. **Jason Sluzevich**: Validation, Data curation. **Olayemi Sokumbi**: Validation, Data curation, Investigation. **Leah Swanson**: Data curation. **Dennis Murphree**: Funding acquisition, Project administration, Resources. **Aaron Mangold**: Conceptualization, Funding acquisition, Project administration, Resources, Supervision, Writing – review & editing. **Ravishankar Iyer**: Funding acquisition, Project administration, Resources, Supervision, Writing – review & editing.

8. Declaration of Competing Interests

The authors state the following competing interests: Aaron Mangold has consulted for Phlecs BV, Kyowa, Eli Lilly, Momenta, UCB, and Regeneron in the past, greater than 24 months ago. He has consulted for Incyte, Soligenix, Clarivate, Argenyx, and Bristol Myers Squibb in the past, less than 12 months ago. He consults for Nuvig, Tourmaline Bio, Janssen, Boehringer Ingelheim currently. He consults for Regeneron and Pfizer currently with payments to the institution. He has grant support from Kyowa, Miragen, Regeneron, Corbus, Pfizer, Incyte, Eli Lilly, Argenx, Palvella, Abbvie, Priovant, Bristol Myers Squibb, Merck in the last 24 months. Beyond 24 months, grant support has come from Sun Pharma, Elorac, Novartis, and Janssen. He has received royalties from Adelphi Values and Clarivate. Aaron Mangold, Ravishankar Iyer, Anirudh Choudhary and Krishnakant Saboo have patent *PCT/US2024/062101* pending to Mayo Foundation for Medical Education and Research and University of Illinois Urbana-Champaign. All other authors have no known competing financial interests or personal relationships that could have appeared to influence the work reported in this paper.

9. Data Statement

Whole-slide image datasets from the TCGA Research Network and the Clinical Proteomic Tumor Analysis Consortium, are publicly available through the NCI Genomic Data Commons Portal (<https://portal.gdc.cancer.gov/>) and the Cancer Imaging Archive (<https://www.cancerimagingarchive.net/>), respectively. These datasets were used to evaluate the performance of RACR-MIL for SCC grading in lung, and head and neck specimens. The in-house skin SCC dataset analyzed in this study is not publicly available due to patient privacy considerations but may be made accessible upon reasonable request to the corresponding author. Access requires submission of a brief research proposal and agreement to a data use policy limited to non-commercial academic research.

Acknowledgments

This work was supported by the Mayo Clinic and Illinois Alliance Fellowship for Technology-based Healthcare Research. This research utilized resources from the National Center for Supercomputing Applications (NCSA), supported by the University of Illinois Urbana-Champaign. We thank Chang Hu, Alysia Hughes, Xing Li, Alyssa Stockard, and Zachary Leibovitz-Reiben for their valuable feedback. Data used in this publication were generated by the National Cancer Institute Clinical Proteomic Tumor Analysis Consortium (CPTAC) and the TCGA Research Network.

References

- Behzadi, M.M., Madani, M., Wang, H., Bai, J., Bhardwaj, A., Tarakanova, A., Yamase, H., Nam, G.H., Nabavi, S., 2024. Weakly-supervised deep learning model for prostate cancer diagnosis and gleason grading of histopathology images. *Biomedical Signal Processing and Control* 95, 106351.
- Burges, C., Shaked, T., Renshaw, E., Lazier, A., Deeds, M., Hamilton, N., Hullender, G., 2005. Learning to rank using gradient descent, in: *Proceedings of the 22nd International Conference on Machine Learning*, Association for Computing Machinery, New York, NY, USA. p. 89–96. URL: <https://doi.org/10.1145/1102351.1102363>, doi:10.1145/1102351.1102363.
- Caron, M., Touvron, H., Misra, I., Jégou, H., Mairal, J., Bojanowski, P., Joulin, A., 2021. Emerging properties in self-supervised vision transformers, in: *Proceedings of the IEEE/CVF international conference on computer vision*, pp. 9650–9660.
- Chan, T.H., Cendra, F.J., Ma, L., Yin, G., Yu, L., 2023. Histopathology whole slide image analysis with heterogeneous graph representation learning, in: *Proceedings of the IEEE/CVF conference on computer vision and pattern recognition*, pp. 15661–15670.

- Chen, R.J., Lu, M.Y., Shaban, M., Chen, C., Chen, T.Y., Williamson, D.F., Mahmood, F., 2021. Whole slide images are 2d point clouds: Context-aware survival prediction using patch-based graph convolutional networks, in: *International Conference on Medical Image Computing and Computer-Assisted Intervention*, Springer. pp. 339–349.
- Cui, Y., Jia, M., Lin, T.Y., Song, Y., Belongie, S., 2019. Class-balanced loss based on effective number of samples, in: *Proceedings of the IEEE/CVF conference on computer vision and pattern recognition*, pp. 9268–9277.
- Diede, C., Walker, T., Carr, D.R., Shahwan, K.T., 2024. Grading differentiation in cutaneous squamous cell carcinoma: a review of the literature. *Archives of Dermatological Research* 316, 434.
- Dominguez-Morales, J.P., Duran-Lopez, L., Marini, N., Vicente-Diaz, S., Linares-Barranco, A., Atzori, M., Müller, H., 2024. A systematic comparison of deep learning methods for gleason grading and scoring. *Medical Image Analysis* 95, 103191.
- Early, J., Cheung, G., Cutajar, K., Xie, H., Kandola, J., Twomey, N., 2024. Inherently interpretable time series classification via multiple instance learning, in: *The Twelfth International Conference on Learning Representations*. URL: <https://openreview.net/forum?id=xriGRsoAza>.
- Edwards, N.J., Oberti, M., Thangudu, R.R., Cai, S., McGarvey, P.B., Jacob, S., Madhavan, S., Ketchum, K.A., 2015. The cptac data portal: a resource for cancer proteomics research. *Journal of proteome research* 14, 2707–2713.
- Gao, J., Aksoy, B.A., Dogrusoz, U., Dresdner, G., Gross, B., Sumer, S.O., Sun, Y., Jacobsen, A., Sinha, R., Larsson, E., et al., 2013. Integrative analysis of complex cancer genomics and clinical profiles using the cbiportal. *Science signaling* 6, p11–p11.
- Gasteiger, J., Weissenberger, S., Günnemann, S., 2019. Diffusion improves graph learning. *Advances in neural information processing systems* 32.
- Geijs, D.J., Dooper, S., Aswolinskiy, W., Hillen, L.M., Amir, A.L., Litjens, G., 2024. Detection and subtyping of basal cell carcinoma in whole-slide histopathology using weakly-supervised learning. *Medical Image Analysis* 93, 103063. URL: <https://www.sciencedirect.com/science/article/pii/S1361841523003237>, doi:<https://doi.org/10.1016/j.media.2023.103063>.
- Hu, Z., Dong, Y., Wang, K., Sun, Y., 2020. Heterogeneous graph transformer, in: *Proceedings of the web conference 2020*, pp. 2704–2710.
- Ilse, M., Tomczak, J., Welling, M., 2018. Attention-based deep multiple instance learning, in: *International conference on machine learning*, PMLR. pp. 2127–2136.
- Kanavati, F., Toyokawa, G., Momosaki, S., Rambeau, M., Kozuma, Y., Shoji, F., Yamazaki, K., Takeo, S., Iizuka, O., Tsuneki, M., 2020. Weakly-supervised learning for lung carcinoma classification using deep learning. *Scientific reports* 10, 9297.
- Li, B., Li, Y., Eliceiri, K.W., 2021. Dual-stream multiple instance learning network for whole slide image classification with self-supervised contrastive learning, in: *Proceedings of the IEEE/CVF conference on computer vision and pattern recognition*, pp. 14318–14328.
- Li, G., Xiong, C., Thabet, A., Ghanem, B., 2020. Deepergcn: All you need to train deeper gcns. *arXiv preprint arXiv:2006.07739*.
- Li, J., Chen, Y., Chu, H., Sun, Q., Guan, T., Han, A., He, Y., 2024. Dynamic graph representation with knowledge-aware attention for histopathology whole slide image analysis, in: *Proceedings of the IEEE/CVF Conference on Computer Vision and Pattern Recognition*, pp. 11323–11332.
- Loshchilov, I., Hutter, F., 2019. Decoupled weight decay regularization, in: *International Conference on Learning Representations*. URL: <https://openreview.net/forum?id=Bkg6RiCqY7>.
- Lu, M.Y., Williamson, D.F., Chen, T.Y., Chen, R.J., Barbieri, M., Mahmood, F., 2021. Data-efficient and weakly supervised computational pathology on whole-slide images. *Nature Biomedical Engineering* 5, 555–570.
- Mun, Y., Paik, I., Shin, S.J., Kwak, T.Y., Chang, H., 2021. Yet another automated gleason grading system (yaaggs) by weakly supervised deep learning. *npj Digital Medicine* 4, 99.
- Myronenko, A., Xu, Z., Yang, D., Roth, H.R., Xu, D., 2021. Accounting for dependencies in deep learning based multiple instance learning for whole slide imaging, in: *International Conference on Medical Image Computing and Computer-Assisted Intervention*, Springer. pp. 329–338.
- Otáloro, S., Marini, N., Müller, H., Atzori, M., 2021. Combining weakly and strongly supervised learning improves strong supervision in gleason pattern classification. *BMC Medical Imaging* 21, 1–14.
- Prezzano, J.C., Scott, G.A., Smith, F.L., Mannava, K.A., Ibrahim, S.F., 2021. Concordance of squamous cell carcinoma histologic grading among dermatopathologists and mohs surgeons. *Dermatologic Surgery* 47, 1433–1437.
- Qin, D., Gammeter, S., Bossard, L., Quack, T., Van Gool, L., 2011. Hello neighbor: Accurate object retrieval with k-reciprocal nearest neighbors, in: *CVPR 2011, IEEE*. pp. 777–784.
- Rogers, H.W., Weinstock, M.A., Feldman, S.R., Coldiron, B.M., 2015. Incidence estimate of nonmelanoma skin cancer (keratinocyte carcinomas) in the us population, 2012. *JAMA dermatology* 151, 1081–1086.
- Shao, Z., Bian, H., Chen, Y., Wang, Y., Zhang, J., Ji, X., et al., 2021. Transmil: Transformer based correlated multiple instance learning for whole slide image classification. *Advances in neural information processing systems* 34, 2136–2147.
- Silva-Rodriguez, J., Colomer, A., Dolz, J., Naranjo, V., 2021. Self-learning for weakly supervised Gleason grading of local patterns. *IEEE Journal of Biomedical and Health Informatics* 25, 3094–3104.
- Sun, S., Tessier, L., Meeuwssen, F., Grisi, C., van Midden, D., Litjens, G., Baumgartner, C.F., 2025. Label-free concept based multiple instance learning for gigapixel histopathology. *arXiv preprint arXiv:2501.02922*.
- Tokez, S., Hollestein, L., Louwman, M., Nijsten, T., Wakkee, M., 2020. Incidence of multiple vs first cutaneous squamous cell carcinoma on a nationwide scale and estimation of future incidences of cutaneous squamous cell carcinoma. *JAMA dermatology* 156, 1300–1306.
- Tomczak, K., Czerwińska, P., Wiznerowicz, M., 2015. Review the cancer genome atlas (tcga): an immeasurable source of knowledge. *Contemporary Oncology/Współczesna Onkologia* 2015, 68–77.
- Tourniaire, P., Ilie, M., Mazières, J., Vigier, A., Ghiringhelli, F., Piton, N., Sabourin, J.C., Bibeau, F., Hofman, P., Ayache, N., et al., 2024. Whario: whole-slide-image-based survival analysis for patients treated with immunotherapy. *Journal of Medical Imaging* 11, 037502–037502.
- Wu, J., Ke, X., Jiang, X., Wu, H., Kong, Y., Shao, L., 2024. Leveraging tumor heterogeneity: Heterogeneous graph representation learning for cancer survival prediction in whole slide images. *Advances in Neural Information Processing Systems* 37, 64312–64337.
- Xiang, J., Wang, X., Wang, X., Zhang, J., Yang, S., Yang, W., Han, X., Liu, Y., 2023. Automatic diagnosis and grading of prostate cancer with weakly supervised learning on whole slide images. *Computers in Biology and Medicine* 152, 106340.
- Yacob, F., Siarov, J., Villiamsson, K., Suvilehto, J.T., Sjöblom, L., Kjellberg, M., Neittaanmäki, N., 2023. Weakly supervised detection and classification of basal cell carcinoma using graph-transformer on whole slide images. *Scientific Reports* 13, 7555.
- Zhang, J., Ma, K., Van Arnem, J., Gupta, R., Saltz, J., Vakalopoulou, M., Samaras, D., 2021. A joint spatial and magnification based attention framework for large scale histopathology classification, in: *Proceedings of the IEEE/CVF Conference on Computer Vision and Pattern*

- Recognition, pp. 3776–3784.
- Zhang, Z., Zhang, H., Zhao, L., Chen, T., Arik, S.Ö., Pfister, T., 2022. Nested hierarchical transformer: Towards accurate, data-efficient and interpretable visual understanding, in: Proceedings of the AAAI Conference on Artificial Intelligence, pp. 3417–3425.
- Zheng, Y., Gindra, R.H., Green, E.J., Burks, E.J., Betke, M., Beane, J.E., Kolachalama, V.B., 2022. A graph-transformer for whole slide image classification. IEEE transactions on medical imaging 41, 3003–3015.

Appendix A. Appendix

Appendix A.1. Model hyperparameter configuration

We summarize the RACR-MIL hyperparameters for the three SCC datasets in Table A.5. For skin SCC and lung SCC, we found that the cosine-softmax classifier yielded the best performance, while for head and neck SCC, the standard softmax classifier performed best. We used 5 nearest neighbors for the latent graph and 8 nearest neighbors for the spatial graph. A single self-attention layer with two heads, one for each graph, was employed. The temperature parameter for the cosine-softmax classifier was optimized separately for each graph configuration. All models were trained using the AdamW optimizer (Loshchilov and Hutter (2019)) with a learning rate of 1×10^{-4} and a batch size of 16. We applied L_2 regularization with a weight of 1×10^{-3} and used a warm-up phase of 10 epochs for the ranking loss, linearly increasing λ_1 from 0 to its target value.

Table A.5: Hyperparameter configuration for RACR-MIL for three SCC datasets

Hyperparameters	Skin SCC			Head & Neck SCC			Lung	
	G_{dual}	G_{lat}	G_{spa}	G_{dual}	G_{lat}	G_{spa}	G_{dual}	G_{lat}
k - latent graph	5	5	5	5	5	5	5	
k - spatial graph	8	8	8	8	8	8	8	
# self-attention layers (Att-GNN)	1	1	1	1	1	1	1	
embedding dimension	64	64	64	64	64	64	64	
dropout	0.5	0.5	0.5	0.5	0.5	0.5	0.5	
τ (cosine classifier)	0.1	0.1	0.1	0.1	0.1	0.1	0.3	
Optimizer parameters								
weight decay	1e-3	1e-3	1e-3	1e-3	1e-3	1e-3	1e-3	
batch size	16	16	16	16	16	16	16	
(β_1, β_2)	0.9, 0.999	0.9, 0.999	0.9, 0.999	0.9, 0.999	0.9, 0.999	0.9, 0.999	0.9, 0.999	0.9, 0.999
learning rate	1e-4	1e-4	1e-4	1e-4	1e-4	1e-4	1e-4	
number of epochs	60	60	60	100	100	100	100	
early stopping epochs	9	9	9	9	9	9	9	
Loss parameters								
λ_1	0.2	0.2	0.2	0.1	0.1	0.1	0.3	
λ_2	0.1	-	-	0.1	-	-	0.1	

Appendix A.2. Precision-recall curves for class-wise performance

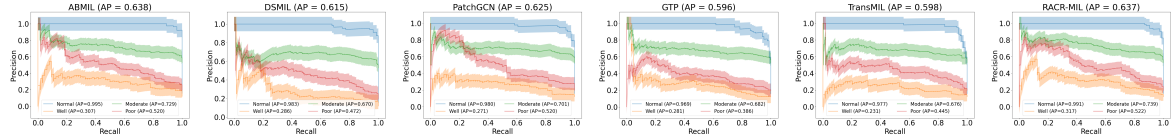


Figure A.13: Precision-recall curves for head and neck SCC grading: RACR-MIL achieves the highest average precision for the three differentiation classes with comparable performance on the Normal class

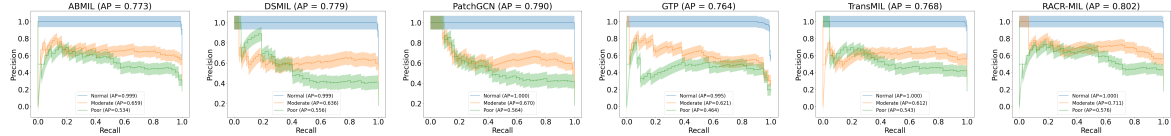


Figure A.14: Precision-recall curves for lung SCC grading: RACR-MIL achieves the highest average precision across all classes.

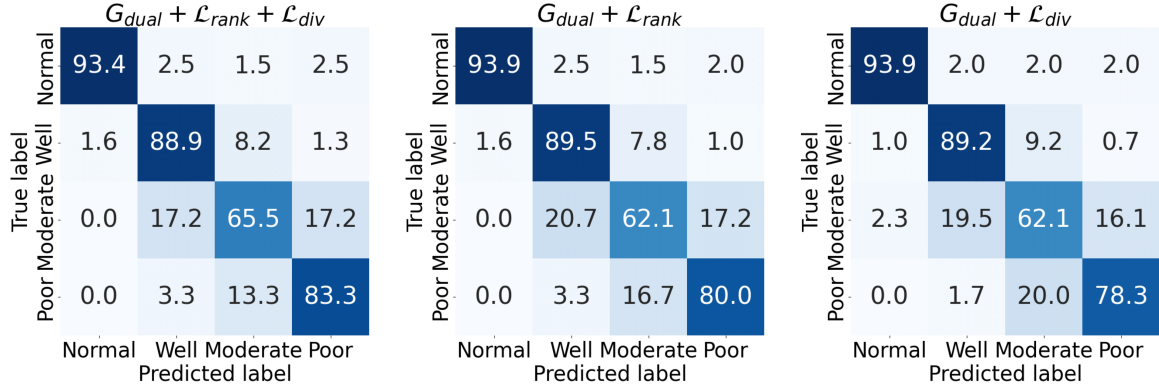


Figure A.15: Confusion matrices for RACR-MIL variants: Incorporating the diversity loss and ranking losses with dual graph formulation leads to the highest accuracy on higher-risk grades.

Appendix A.3. Code

The code to reproduce our experiments, along with the pretrained patch features, will be made publicly available at https://www.github.com/anici46/racr_mil following the completion of the review process.